Electrocatalysis

Deutsche Ausgabe: DOI: 10.1002/ange.201508809
Internationale Ausgabe: DOI: 10.1002/anie.201508809

A Strategy to Promote the Electrocatalytic Activity of Spinels for Oxygen Reduction by Structure Reversal

Guangping Wu, Jun Wang, Wei Ding, Yao Nie, Li Li,* Xueqiang Qi, Siguo Chen, and Zidong Wei**

Abstract: *The electrocatalytic performance of a spinel for the oxygen reduction reaction (ORR) can be significantly promoted by reversing its crystalline structure from the normal to the inverse. As the spinel structure reversed, the activation and cleavage of O–O bonds are accelerated owing to a dissimilarity effect of the distinct metal atoms co-occupying octahedral sites. The* $Co^{II}Fe^{III}Co^{III}O_4$ *spinel with the Fe and Co co-occupying inverse structure exhibits an excellent ORR activity, which even exceeds that of the state-of-the-art commercial Pt/C by 42 mV in alkaline medium.*

The development of high-performance and low-cost catalytic materials for the oxygen reduction reaction (ORR) has been a major challenge for the large-scale application of fuel cells.[1] So far, the platinum-based materials have been the best ORR electrocatalyst;[2] but they cannot meet the requirement of widespread commercialization of fuel cells owing to their high price and scarcity. The ultimate way to address this issue is to exploit low-cost non-precious ORR electrocatalysts.[3] Among noble-metal-free alternatives, spinel materials, such as Co_3O_4 and $MnCo_2O_4$, have received much attention because of their high element abundance, low cost, and low environmental impact.[4] Nevertheless, to replace platinum, the spinel ORR activities are still less competitive. Strategies to enhance spinel activity include doping with cations, coating with metals, integrating conductive nanostructures, and introducing oxygen defects.[5] Although these approaches have been proven to be effective, further promotion of their ORR activity is still necessary.

Herein, we report that, for the first time, the ORR catalytic activity of spinel can be significantly enhanced by reversing the spinel crystalline structure from normal to inverse. It is well known that the normal spinel structure, with general formula AB_2X_4, is a cubic close-packed array of X^{2-} ions with the A and B ions occupying the interstices.[6] The A atoms occupy the tetrahedral sites and the B atoms occupy the octahedral sites. Thus, the normal spinel can be written as $\{A\}[B_2]X_4$, where the braces "{}" represent the tetrahedral site occupations and the brackets "[]" represent the octahedral site occupations. According to a site preference theory,[6] if {B}[A] is more stable than {A}[B], the $\{A\}[B_2]X_4$ will be changed to its inverse spinel structure, that is, $\{B\}[A][B]X_4$. It means that all the A atoms and one-half of the B atoms have exchanged places. In Co-Fe spinel oxides, there is a possibility to form an inverse spinel structure, that is, $\{B\}[A][B]X_4$, as long as Fe and Co atoms co-share the octahedral sites.[7]

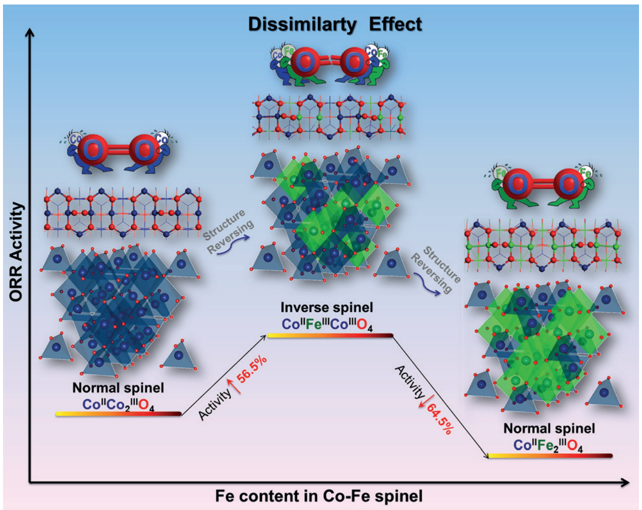

Figure 1. The spinel structures of $\{Co\}[Co_2]O_4$, $\{Co\}[FeCo]O_4$, and $\{Co\}[Fe_2]O_4$ and the corresponding oxygen adsorptions and ORR activities (Fe green, Co blue, absorbed O magenta, lattice O red).

Herein, to reveal the structural effect on spinel electrocatalytic performance, we tuned a Co-Fe based spinel structure from its normal to the inverse and then back to its normal by adjusting the iron content in the synthesis. Figure 1 illustrates the structures of as-prepared Co-Fe based spinel. With iron content increase, the spinel structures vary from the normal spinel structure as $\{Co\}[Co_2]O_4$ to the inverse as $\{Co\}[FeCo]O_4$, and eventually to the normal spinel structure as $\{Co\}[Fe_2]O_4$. After being supported on nitrogen-doped graphene, these spinel materials exhibit different ORR activities in alkaline medium. Among them, the $\{Co\}[FeCo]O_4$/NG with an inverse structure shows the highest ORR activity, which is even better than the state-of-the-the art commercial Pt/C in the half-wave potential ($E_{1/2}$) by 42 mV. Density functional theory (DFT) calculations show that the higher ORR activity of the inverse spinel $\{Co\}[FeCo]O_4$ originates from the dissimilarity effect of Fe and Co atoms at the octahedral site, which modulates the oxygen

---

[*] Dr. G. Wu, Dr. J. Wang, Dr. W. Ding, Dr. Y. Nie, Prof. L. Li, Dr. X. Qi, Dr. S. Chen, Prof. Z. Wei
Chongqing Key Laboratory of Chemical Process for Clean Energy and Resource Utilization, School of Chemistry and Chemical Engineering
Chongqing University, Shapingba 174, Chongqing (China)
E-mail: dingwei128@cqu.edu.cn
liliracial@cqu.edu.cn
zdwei@cqu.edu.cn

Supporting information and ORCID(s) from the author(s) for this article are available on the WWW under http://dx.doi.org/10.1002/anie.201508809.

adsorption energy (E_{ad}) and elongates the adsorbed oxygen bond compared to that on the normal spinel.

The crystal structures of the synthesized Co-Fe based materials were confirmed by using X-ray diffraction analysis (XRD), as shown in Figure 2a. The well-defined diffraction patterns with diffraction peaks corresponding to (111), (220), (311), (222), (400), (422), (511), and (440) crystal planes, respectively, indicate a highly crystalline cubic spinel structure for the synthesized Co-Fe based materials.[8] The diffraction patterns for as-made {Co}[Co_2]O_4 and {Co}[Fe_2]O_4 match those for the standard Co_3O_4 and $CoFe_2O_4$, confirming the normal spinel structures of the as-made {Co}[Co_2]O_4 and {Co}[Fe_2]O_4. The shift of diffraction peaks to a smaller 2θ angle position indicates the expansion of crystalline structure with Fe^{3+} ions substituting Co^{3+} ions in octahedral sites. This is because Fe^{3+} ions (0.65 Å) is larger than Co^{3+} ions (0.61 Å).[9] The average particle size for {Co}[Co_2]O_4, {Co}[FeCo]O_4, and {Co}[Fe_2]O_4 is 22.3, 14.9, and 17.7 nm, respectively (calculated by using the Debye–Scherrer equation from XRD results). This calculated particle size is consistent with the observation based on the transmission electron microscope (TEM) images (Supporting Information, Table S1). The TEM images show the spinel nanoparticles with a diameter of about 20 nm uniformly dispersed on the surface of N-doped graphene (Figure 2b–d; Supporting Information, Figure S1). The high-resolution TEM images in Figure 2e–g show the distinct lattice (220) fringes of 0.286, 0.293, and 0.297 nm for {Co}[Co_2]O_4, {Co}[FeCo]O_4, and {Co}[Fe_2]O_4, respectively, which further confirms the expansion of crystalline structure with Fe^{3+} ions substituting Co^{3+} ions in octahedral sites.

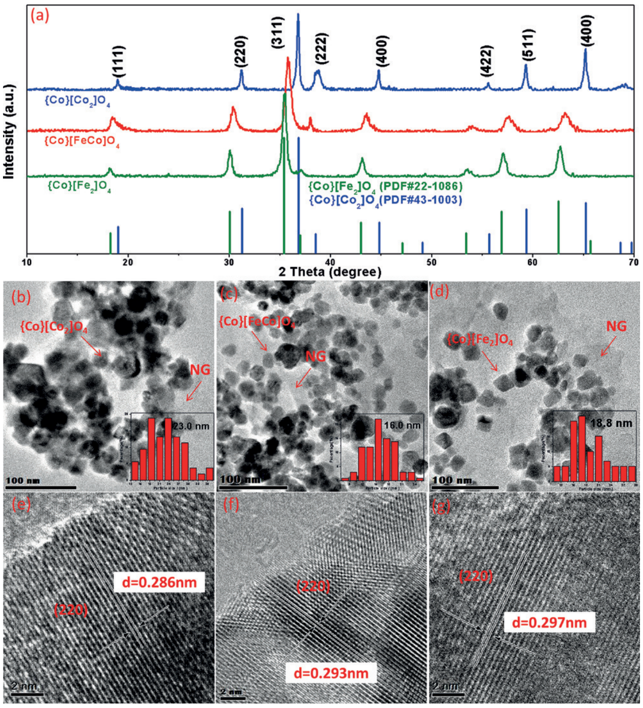

Figure 2. a) X-ray diffraction patterns ($Cu_{K\alpha}$ radiation) of {Co}[Co_2]O_4, {Co}[FeCo]O_4, and {Co}[Fe_2]O_4 nanoparticles. b) g) TEM and particle-distribution histograms and HRTEM images of {Co}[Co_2]O_4/NG (b and e), {Co}[FeCo]O_4/NG (c and f), and {Co}[Fe_2]O_4/NG (d and g).

The Co 2p X-ray photoelectron spectroscopy (XPS) spectrum (Supporting Information, Figure S2) shifts to lower binding energy and decreases in intensity with the decrease of the Co content in the order of {Co}[Co_2]O_4, {Co}[FeCo]O_4, and {Co}[Fe_2]O_4. The Co 2p XPS spectrum splits into $2p_{1/2}$ and $2p_{3/2}$ components at 780.0 eV and 795.5 eV, respectively. To avoid the obstruction of Auger signals from Fe, the analysis of the Co chemical state was based on the Co $2p_{1/2}$ spectra. In the XPS spectra of {Co}[Co_2]O_4 and {Co}[FeCo]O_4, Co $2p_{1/2}$ can be fitted as two distinct peaks at the lower binding energy for Co^{2+} state and at higher for Co^{3+} state.[10] The atomic ratio of Co^{2+} to Co^{3+} is 0.485 and 1.00 for {Co}[Co_2]O_4 and {Co}[FeCo]O_4, respectively, which nearly matches the atomic ratio in {Co^{II}}[Co_2^{III}]O_4 and {Co^{II}}[$Co^{III}Fe^{III}$]O_4 spinel. For the {Co}[Fe_2]O_4, the Co $2p_{1/2}$ spectrum has one peak at the binding energy of 795.4 eV, indicating the absences of Co^{3+}. The peak positions of Fe 2p XPS spectra (Supporting Information, Figure S3) in {Co}[Fe_2]O_4 (710.2 eV) and {Co}[FeCo]O_4 (709.9 eV) closely match that of Fe in Fe_2O_3 (710.4 eV).[11] It confirms that the Fe species exist as Fe^{III} state in both of {Co}[Fe_2]O_4 and {Co}[FeCo]O_4. The bulk Fe/Co atom ratio, analyzed by using energy-dispersive X-ray spectroscopy (EDX), is 0.503 and 1.93 for {Co}[FeCo]O_4 and {Co}[Fe_2]O_4, respectively (Supporting Information, Figure S4 and Table S2). These results confirm that the as-prepared spinel structures are well agreement with those presented in Figure 1.

The electrocatalytic activities of the as-prepared catalysts toward the ORR were examined by using linear sweep voltammetry (LSV) in an O_2-saturated 0.1 M KOH solution at a rotational rate of 1600 rpm (Figure 3). The electrocatalytic activities, as estimated from $E_{1/2}$, are maximized for {Co}[FeCo]O_4/NG and decrease successively for {Co}[Co_2]O_4/NG, {Co}[Fe_2]O_4/NG and Pt/C, with $E_{1/2}$ values of 866, 846, 824, and 824 mV (versus the reversible hydrogen electrode, RHE), respectively. The same order of the kinetic current densities

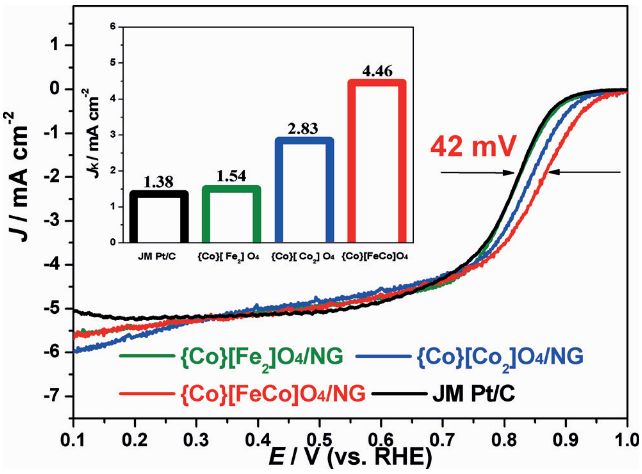

Figure 3. LSVs of {Co}[Fe_2]O_4/NG, {Co}[Co_2]O_4/NG, {Co}[FeCo]O_4/NG, and Pt/C, and corresponding J_K (inset) at 0.85 V vs. RHE in an O_2-saturated 0.1 M KOH solution at 1600 rpm. $\nu = 10$ mV s^{-1}. Non-Pt catalyst loading: 0.6 mg cm^{-2}; Pt loading: 20 µg Pt cm^{-2}.

(J_k) are also observed for these catalysts at 0.85 V vs. RHE according to the Koutecky–Levich (K-L) equation; that is, $\{Co\}[FeCo]O_4$/NG (4.46 mA cm^{-2}) > $\{Co\}[Co_2]O_4$/NG (2.83 mA cm^{-2}) > $\{Co\}[Fe_2]O_4$/NG (1.54 mA cm^{-2}) > Pt/C (1.35 mA cm^{-2}) (Figure 3, inset). The Tafel slopes (Supporting Information, Figure S5) are smallest on $\{Co\}[FeCo]O_4$/NG-modified electrode, and increased in the order of Pt/C-, $\{Co\}[Co_2]O_4$/NG-, and $\{Co\}[Fe_2]O_4$/NG-modified electrode. The transferred electron number, determined from the K-L plots in the Supporting Information, Figure S6, is 3.6, 3.9, and 3.8 for $\{Co\}[Fe_2]O_4$/NG, $\{Co\}[FeCo]O_4$/NG, and $\{Co\}[Co_2]O_4$/NG, respectively, indicating a four-electron pathway for the catalysis of ORR. Among the as-prepared spinel catalysts, the $\{Co\}[FeCo]O_4$/NG catalyst exhibits the most positive onset potential (980 mV) and $E_{1/2}$ (866 mV) for ORR, which exceed the corresponding potentials of the commercial Pt/C by 65 and 42 mV, respectively. It indicates that $\{Co\}[FeCo]O_4$/NG catalyst with the inverse spinel structure is a much better catalyst than the Pt/C for the ORR. As being aware of the contribution of NG support to the catalysis of the ORR, we evaluated the ORR activities of NG and as-made spinel materials separately. As shown in the Supporting Information, Figure S7, the highest ORR activity and smallest Tafel plots among the different spinel materials are observed for $\{Co\}[FeCo]O_4$ and the ORR activities decrease in the order $\{Co\}[Co_2]O_4 > \{Co\}[Fe_2]O_4$. These results indicate that the main contribution to the spinel ORR activity enhancement comes from the structural effect of spinel. Furthermore, the outperformance of $\{Co\}[FeCo]O_4$/NG compared to $\{Co\}[FeCo]O_4$ or NG alone indicates a synergistic catalysis effect between NG support and spinel. Along with demonstrating that the $\{Co\}[FeCo]O_4$/NG catalysts exhibited relatively high ORR activities, we also evaluated the stability of the $\{Co\}[FeCo]O_4$/NG catalysts by chronoamperometric at the potential of 0.8 V vs. RHE. As shown in the Supporting Information, Figure S8, the cathodic current density decreases by less than 37 % of initial state over 5.5 h of continuous operation on the $\{Co\}[FeCo]O_4$/NG catalyst catalyzed electrode, while the cathodic current density decreased by more than 48 % on the Pt/C catalyst catalyzed electrode, indicating a better stability of $\{Co\}[FeCo]O_4$/NG. Besides, the $\{Co\}[FeCo]O_4$/NG exhibits high selectivity toward the ORR with a remarkable tolerance for methanol (Supporting Information, Figure S9).

To gain further insight into the relationships between ORR activity and catalyst structures, we conducted DFT calculations to study the adsorption and dissociation of oxygen at the sites on the spinel (110) surface. The octahedral sites are selected for the theoretical investigation because they are the major difference between the normal and the inverse. As shown in Figure 4, there are two adsorption patterns. One is the duel pattern where O_2 molecule is adsorbed on two octahedral atoms, and another is the triangle pattern where O_2 molecule is adsorbed among one tetrahedral atom and two octahedral atoms. With a replacement of a half or the whole octahedral site Co atoms by Fe atoms, the normal spinel $\{Co\}[Co_2]O_4$ transforms into the inverse spinel $\{Co\}[FeCo]O_4$, or normal spinel $\{Co\}[Fe_2]O_4$, respectively. For both adsorption patterns, the E_{ad} does not change much from the normal spinel $\{Co\}[Co_2]O_4$ to the inverse spinel $\{Co\}[FeCo]O_4$. However, the O–O bonds adsorbed on $\{Co\}[FeCo]O_4$ are lengthened from 1.354 Å to the range of 1.360 to 1.369 Å in comparison with that on $\{Co\}[Co_2]O_4$ in the case of the duel pattern, and from 1.420 Å to the range of 1.438 to 1.436 Å in the case of triangle pattern, respectively. It means the O–O bond of adsorbed O_2 on $\{Co\}[FeCo]O_4$ is more activated than that on $\{Co\}[Co_2]O_4$. What is more, with a full replacement of Co atoms by Fe at octahedral sits, and the inverse spinel $\{Co\}[FeCo]O_4$ turning back to the normal spinel $\{Co\}[Fe_2]O_4$, the adsorption energy of oxygen drops to −0.486 eV in the case of the duel pattern, but keeps the same level as before (3.220 eV) in the case of the triangle pattern. It means that there is a poor adsorption of O_2 on $\{Co\}[Fe_2]O_4$ in the case of the duel pattern; and therefore, it is difficult for the O–O bond of adsorbed O_2 on $\{Co\}[Fe_2]O_4$ to be activated in

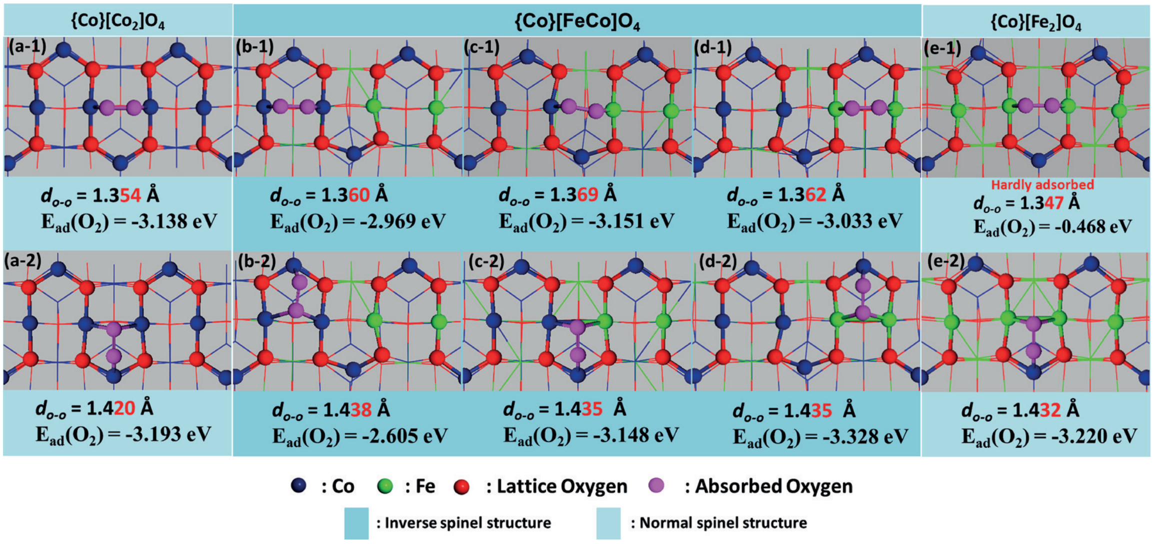

Figure 4. The O–O bond length and adsorption energy of oxygen adsorbed in duel pattern (top) and triangle pattern (bottom) of a) $\{Co\}[Co_2]O_4$, b)–d) $\{Co\}[FeCo]O_4$, and e) $\{Co\}[Fe_2]O_4$.

the case of the duel pattern. As shown in Figure 4, only on the inverse spinel {Co}[FeCo]O_4 the values of $d_{\text{O−O}}$ is lengthened to 1.36 Å or more. It indicates that the oxygen is easier to be activated on the inverse spinel {Co}[FeCo]O_4 than on the normal spinel regardless of {Co}[Co_2]O_4 or {Co}[Fe_2]O_4, explaining why the best ORR activity was observed on the inverse spinel {Co}[FeCo]O_4. Furthermore, with the matching adsorption energy, the O−O bond adsorbed on the inverse spinel {Co}[FeCo]O_4 is always slightly longer than that on the normal spinel {Co}[Co_2]O_4 or {Co}[Fe_2]O_4 (Supporting Information, Table S3). This indicates that there certainly has another factor along with the adsorption pattern that influences the O−O bond activation. We propose that the different octahedral metal atoms should be associated with the accelerating effect in the activation and cleavage of O−O bonds.

The different octahedral metal atoms promote charge polarization between them, which further favors the adsorption and dissociation of O_2. We define these changes caused by different atoms as a dissimilarity effect. As shown in Figure 5, with the normal spinel reversing to inverse spinel, the electronic balance on the octahedral atoms is broken and charge polarization occurs between the octahedral atoms, that is, Co and Fe. At the same time, with the spinel experiencing normal, inverse, and normal structure, subsequently, both the lattice parameter and the Fermi energy reach to a modest level in the case of inverse spinel. As is well-known, the high Fermi energy of the electrocatalysts is conducive for O_2 adsorption but detrimental for the desorption of an adsorbed O atom.[12] There also is an optimum distance for two active sites in the duel adsorption pattern.[13] Therefore, holding a modest Fermi energy and lattice parameter is why the inverse spinel {Co}[FeCo]O_4 shows the best ORR activity in all cases. These results indicate that as long as the electronic or structural polarization occurs, sites that favor O_2 sorption and dissociation are created, and spinels will be a highly active ORR electrocatalysts. We imagine that such a dissimilarity effect may also occur in the oxygen evolution reaction (OER) because the OER is also associated with the oxygen-containing species adsorption and desorption process. Therefore, the OER activities in alkaline medium were evaluated. As speculated, the OER activities on the inverse/normal spinel catalysts follow the same order as that of their ORR activities, that is, the higher ORR activity, the higher OER activity also (Supporting Information, Figure S10).

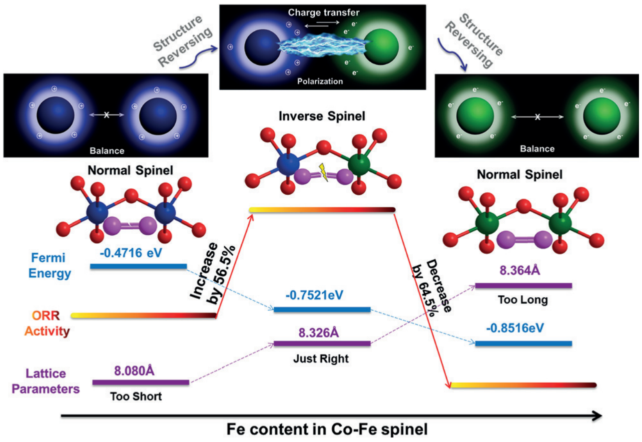

Figure 5. Representation showing the dissimilarity effect and polarization of octahedral atoms and the relationships between ORR activity and Fermi energy or lattice parameters (Fe green, Co blue, absorbed O magenta, lattice O red).

In summary, we have demonstrated that the electrocatalytic performance of the Co-Fe based spinel for the catalysis of ORR can be significantly promoted by reversing its structure from the normal to the inverse by adjusting iron content in the spinel. The inverse {Co}[FeCo]O_4 spinel exhibits the highest ORR activity among all spinel structures, and exceeds that of the state of art commercial Pt/C by 42 mV in alkaline medium. DFT calculations reveal that the enhancement of intrinsic ORR activity on {Co}[FeCo]O_4 originates from the so-called dissimilarity effect of Fe and Co atoms at the octahedral sites, which modulates the E_{ad} and elongates O−O bonds compared to that of the normal spinel. This work opens a new way for modulating the catalytic activity of spinel for industrial purposes that range from catalysis and sensors to supercapacitors and lithium-ion batteries.

Acknowledgements

This work was financially supported by the China National 973 Program (2012CB215500 and 2012CB720300) and by the NSFC of China (Grant Nos. 91534205, 21436003, 21573029, and 21576032).

Keywords: dissimilarity effect · electrocatalysis · inverse spinels · oxygen reduction reaction

How to cite: *Angew. Chem. Int. Ed.* **2016**, *55*, 1340–1344
Angew. Chem. **2016**, *128*, 1362–1366

---

[1] W. Ding, Z. D. Wei, S. G. Chen, X. Q. Qi, T. Yang, J. S. Hu, D. Wang, L. J. Wan, S. M. Alvi, L. Li, *Angew. Chem. Int. Ed.* **2013**, *52*, 11755–11759; *Angew. Chem.* **2013**, *125*, 11971–11975.

[2] a) H. A. Gasteiger, S. S. Kocha, B. Sompalli, F. T. Wagner, *Appl. Catal. B* **2005**, *56*, 9–35; b) X. Liu, H. M. Wang, S. G. Chen, X. Q. Qi, H. L. Gao, Y. Hui, Y. Bai, L. Guo, W. Ding, Z. D. Wei, *J. Energy Chem.* **2014**, *23*, 358–362; c) W, Li, W. Ding, G. P. Wu, J. H. Liao, Y. Nie, X. Q. Qi, L. Li, S. G. Chen, Z. D. Wei, *Chem. Eng. Sci.* **2015**, *135*, 45–51.

[3] a) A. Kloke, F. von Stetten, R. Zengerle, S. Kerzenmacher, *Adv. Mater.* **2011**, *23*, 4976–5008; b) Y. J. Feng, N. Alonso-Vante, *Phys. Status Solidi B* **2008**, *245*, 1792–1806; c) Z. W. Chen, D. Higgins, A. Yu, L. Zhang, J. J. Zhang, *Energy Environ. Sci.* **2011**, *4*, 3167–3192; d) R. Cao, J. S. Lee, M. Liu, J. Cho, *Adv. Energy Mater.* **2012**, *2*, 816–828; e) F. Cheng, J. Chen, *Chem. Soc. Rev.* **2012**, *41*, 2172–2192.

[4] a) Y. Y. Liang, Y. G. Li, H. L. Wang, J. G. Zhou, J. Wang, T. Regier, H. J. Dai, *Nat. Mater.* **2011**, *10*, 780–786; b) S. C. Ma, L. Q. Sun, L. N. Cong, X. G. Gao, C. Yao, X. Guo, L. H. Tai, P. Mei, Y. P. Zeng, H. M. Xie, R. S. Wang, *J. Phys. Chem. C* **2013**, *117*, 25890–25897; c) M. Hamdani, R. N. Singh, P. Chartier, *Int. J. Electrochem. Sci.* **2010**, *5*, 556–577.

[5] a) J. X. Li, M. Z. Zou, W. W. Wen, Y. Zhao, Y. B. Lin, L. Z. Chen, H. Lai, L. H. Guan, Z. G. Huang, *J. Mater. Chem. A* **2014**, *2*, 10257 – 10262; b) H. Y. Zhu, S. Zhang, Y.-X. Huang, L. H. Wu, S. H. Sun, *Nano Lett.* **2013**, *13*, 2947 – 2951; c) F. Y. Cheng, T. R. Zhang, Y. Zhang, J. Du, X. P. Han, J. Chen, *Angew. Chem. Int. Ed.* **2013**, *52*, 2474 – 2477; *Angew. Chem.* **2013**, *125*, 2534 – 2537; d) J. Bao, X. D. Zhang, B. Fan, J. J. Zhang, M. Zhou, W. L. Yang, X. Hu, H. Wang, B. C. Pan, Y. Xie, *Angew. Chem. Int. Ed.* **2015**, *54*, 7399 – 7400; *Angew. Chem.* **2015**, *127*, 7507 – 7512.

[6] F. Y. Cheng, J. Shen, B. Peng, Y. D. Pan, Z. L. Tao, J. Chen, *Nat. Chem.* **2011**, *3*, 79 – 84.

[7] J. K. Burdett, G. D. Price, S. L. Price, *J. Am. Chem. Soc.* **1982**, *104*, 92 – 95.

[8] S. Ayyappan, S. Mahadevan, P. Chandramohan, M. P. Srinivasan, J. Philip, B. Raj, *J. Phys. Chem. C* **2010**, *114*, 6334 – 6341.

[9] R. Ning, J. Q. Tian, A. M. Asiri, A. H. Qusti, A. O. Al-Youbi, X. P. Sun, *Langmuir* **2013**, *29*, 13146 – 13151.

[10] N. Ballarini, F. Cavani, S. Passeri, L. Pesaresi, A. F. Lee, K. Wilson, *Appl. Catal. A* **2009**, *366*, 184 – 192.

[11] a) J. Liu, X. J. Sun, P. Song, Y. W. Zhang, W. Xing, W. L. Xu, *Adv. Mater.* **2013**, *25*, 6879 – 6883; b) V. I. Nefedov, Y. V. Salyn, G. Leonhardt, R. Scheibe, *J. Electron Spectrosc. Relat. Phenom.* **1977**, *10*, 121 – 124.

[12] a) M. Ptasinska, J. Piechota, S. Krukowski, *J. Phys. Chem. C* **2015**, *119*, 11563 – 11569; b) C. Y. Jia, W. L. Fan, F. Yang, X. Zhao, H. G. Sun, P. Li, L. Liu, *Langmuir* **2013**, *29*, 7025 – 7037; c) D. H. Deng, L. Yu, X. Q. Chen, G. X. Wang, L. Jin, X. L. Pan, J. Deng, G. Q. Sun, X. H. Bao, *Angew. Chem. Int. Ed.* **2013**, *52*, 371 – 375; *Angew. Chem.* **2013**, *125*, 389 – 393.

[13] W. W. Zhang, L. Li, W. Ding, S. G. Chen, H. M. Wang, Z. D. Wei, *J. Mater. Chem. A* **2014**, *2*, 10098 – 10103.

Received: September 20, 2015